Strong metal–support interaction improves activity and stability of Pt electrocatalysts on doped metal oxides†

Ignacio Jiménez-Morales, Sara Cavaliere, * Deborah Jones and Jacques Rozière

Niobium and antimony doped tin oxide loose-tubes decorated with Pt nanoparticles present outstanding mass activity and stability, exceeding those of a reference carbon-based electrocatalyst. Physico-chemical characterisation and in particular X-ray photoelectron spectroscopy demonstrate that this observation can be ascribed to the strong metal–support interaction promoting electroactivity and Pt anchoring on doped metal oxide supports.

Introduction

Metal oxides are attractive materials for applications requiring oxidative conditions for instance as electrocatalyst supports in fuel cell cathodes, due to their chemical and electrochemical stability against corrosion.[1–3] Furthermore, they often promote the electrocatalytic activity of metal catalysts towards the reactions taking place, *i.e.* the oxygen reduction reaction (ORR).[4,5] This phenomenon is ascribed to the so-called strong metal–support interaction (SMSI)[6,7] evidence for which is generally deduced from X-ray diffraction (XRD) and X-ray Photoelectron Spectroscopy (XPS) characterisation.[8–10] The main drawback of metal oxides in the context of fuel cell electrode materials is their semiconductor behaviour and the subsequent limited electronic conductivity, that is often circumvented by formation of composite or mixed materials with carbon[4,11–13] or doping with aliovalent ions.[14–16] Among the various metal oxides investigated as electrocatalyst supports alternative to carbon, tin oxide has attracted particular research attention.[17] Several nanostructured materials based on SnO_2 have been synthesised, doped mainly with niobium[18–23] and antimony[12,19,21,24–26] ions, eventually added to carbonaceous materials[12,13,27–31] and characterised as platinum supports for ORR electrocatalysis. The higher corrosion resistance of this kind of supported electrocatalyst at high potential (up to 1.2–1.5 V) compared to carbon-based materials has been thoroughly demonstrated.[20,22,24,26,27,31–37] For instance, Pt deposited onto antimony doped tin oxide (ATO) nanoparticles, when submitted to 800 cycles between 0.6 and 1.2 V, showed an ORR activity decrease of 35% *vs.* the 78% observed for Pt/C, and a similar relative decrease in electrochemical surface area (ECSA) of 36% compared to the 80% for Pt/C.[24]

Nevertheless, despite this significant improvement in corrosion resistance, the electroactivity reached so far by Pt/doped-SnO_2 catalysts is still far from meeting the target of 0.44 A mg^{-1} Pt at 0.9 V *vs.* RHE.[38] For instance, mass activity values of 1.55 A mg^{-1} Pt at 0.8 V per RHE,[18] 0.95 A mg^{-1} Pt at 0.85 V per RHE[39] and 0.08 A mg^{-1} Pt at 0.9 V per RHE[23] were reported for Pt nanoparticle catalysed Nb doped SnO_2 (NTO).

Herein, we present our work on niobium and antimony doped tin oxide loose-tubes prepared by electrospinning and decorated with Pt nanoparticles obtained by a microwave-assisted polyol method. Previously, we have reported the synthesis and the *ex situ* and *in situ* electrochemical characterisation of these materials, and demonstrated their stability at potentials as high as 1.4 V.[20,36,37,40] However, low ECSA (*ca.* 30 $m^2\ g^{-1}$)[37,40] and activity (0.034 A mg^{-1} Pt for Pt/NTO[36] and 0.14 A mg^{-1} Pt for Pt/ATO[37] at 0.9 V per RHE) were observed, that we ascribed in particular to the low and/or inhomogeneous electronic conductivity of the metal oxide supports.

We describe here the further development of these electrocatalysts that has led to remarkably high activity towards the oxygen reduction reaction and stability at high potential. Furthermore, detailed XPS investigation has shed light on the origin of these improved properties that are attributed to a strong interaction between Pt and doped SnO_2.

Experimental

Synthesis of Sb and Nb doped SnO_2 loose-tubes

Doped tin oxides were prepared by electrospinning followed by thermal treatment, and their doping amounts (5 at% Nb and

Institut Charles Gerhardt Montpellier, UMR CNRS 5253, Agr'egats Interfaces et Mat'eriaux pour l'Energie, Universit'e de Montpellier, 34095 Montpellier Cedex 5, France. E-mail: sara.cavaliere@umontpellier.fr

† Electronic supplementary information (ESI) available. See DOI: 10.1039/c8cp00176f

10 at% Sb) were those leading to the maximum electrical conductivity.[37,40] The synthesis of the doped SnO_2 fibre-in-tubes was performed as reported elsewhere.[37,40] The obtained samples were labelled NTO (5 at% niobium doped tin oxide) and ATO (10 at% antimony doped tin oxide).

Synthesis of Pt/doped-SnO_2

Pt nanocatalyst particles were synthesised using a microwave-assisted polyol method[16] that was modified to obtain nanoparticles with slightly larger size and with a polyol-free surface. Hexachloroplatinic acid (133 mg, 99.9% Alfa Aesar) was dissolved in ethylene glycol (EG, 108 mL, 99.8%, Sigma Aldrich) and the pH was adjusted to 11.4 with NaOH (1 M solution in EG, 98%, Sigma Aldrich). The obtained solution was heated at 165 °C for 8 minutes, and then for 39 seconds at 160 W in a microwave reactor (MiniFlow 200SS Sairem). The doped-SnO_2 materials (60 mg) were added to the resulting Pt nanoparticle suspension while lowering the pH to 2 using H_2SO_4 (1 M solution in EG, 95–98%, Sigma Aldrich). The suspension was stirred for 24 hours, and then the Pt/doped-SnO_2 was recovered by filtration, washed with Milli-Q® grade water and ethanol, and dried at 80 °C for 24 h. A further thermal treatment at 160 °C for one hour was performed to remove any EG traces from the Pt surface. The same Pt nanoparticle synthesis and deposition was repeated on Vulcan XC-72R (Cabot), to obtain Pt/C materials for a comparative X-ray photoelectron spectroscopy analysis.

Physico-chemical characterisation of doped-SnO_2 and Pt/doped-SnO_2

The morphology of the Pt/doped-SnO_2 materials was analysed by transmission electron microscopy (TEM) using a JEOL 1200 EXII microscope operating at 120 kV equipped with a CCD camera SIS Olympus Quemesa (11 million pixels). Samples were suspended in ethanol and sonicated, then deposited onto carbon-coated copper grids. The average sizes of Pt and doped-SnO_2 materials were determined by measuring 200 selected objects using the ImageJ software.

Powder X-ray diffraction (XRD) patterns were recorded at 20 °C in Bragg–Brentano configuration using a PANalytical X'pert diffractometer, equipped with a hybrid monochromator, operating with CuK_α radiation (λ = 1.541 Å). A step size of 0.1° 2θ within the 2θ domain from 20 to 80° was employed.

X-ray fluorescence (XRF) was used to determine the Pt loading on doped-SnO_2. Samples were prepared by grinding 50 mg of each electrocatalyst with 25 mg of cellulose. The recovered powder was placed in a cavity in an H_3BO_3 matrix and subsequently pressed to obtain a pellet of 32 mm diameter with scanned surface of *ca.* 12 mm. The same protocol was used to prepare seven standards using 15, 20, 25, 30, 35, 40 and 45 wt% of Pt black (Alfa Aesar) and doped-SnO_2 to obtain a calibration line. The XRF analyses were performed with a PANalytical Axios Max spectrometer fitted with a Rh (4 kW) tube, and equipped with a LiF200 crystal and Omnian software.

The surface chemical state of the materials was investigated by X-ray Photoelectron Spectroscopy (XPS) on an ESCALAB 250 (Thermo Electron). The X-ray excitation was provided by a monochromatic Al K_α (1486.6 eV) source and the analysed surface area was 400 mm^2. A constant analyser energy mode was used for the electron detection (20 eV pass energy). Detection of the emitted photoelectrons was performed perpendicular to the simple surface. Data quantification was performed in the Avantage software, removing the background signal using the Shirley method. The surface atomic concentrations were determined from photoelectron peak areas using the atomic sensitivity factors reported by Scofield. Binding energies of all core levels are referred to the C–C bond of C1s at 284.8 eV.

Electrochemical characterisation of Pt/Sb-SnO_2

The electrochemical analyses were carried out at 20 °C using a Pine bipotentiostat model AFCBP1 in a conventional three-electrode cell (reversible hydrogen electrode (RHE, reference electrode), glassy carbon rotating disk electrode (RDE) (working electrode, geometric area 0.196 cm^2), and platinum wire (counter electrode)). All the potential values are referred to the RHE and the current densities are reported as current per geometric electrode area. In order to prepare the catalyst ink, 5 mg of the Pt/doped SnO_2 electrocatalyst were dispersed in 613 µL (554 µL) of Milli-Q® grade water, 2.5 mL (2.2 mL) of ethanol (Aldrich) and 22 µL (19 µL) 5 wt% Nafion® EW1100 solution in alcohols (Aldrich). For the reference, 5.3 mg of 57 wt% Pt/C (HiSPEC 9100 from Johnson Matthey, 2.6 nm particle size measured by TEM) were mixed with 1 mL of Milli-Q® grade water, 4 mL of ethanol (Aldrich) and 35 µL of the 5 wt% Nafion® EW 1100 solution in alcohols (Aldrich). Catalyst inks were sonicated (VWR Ultrasonic Cleaner) for 5 min. Aliquots of 7 µL of the inks were then deposited onto the RDE surface with a micropipette and dried in air. The Pt loading onto the electrode was 21.3 µg cm^{-2} for all electrocatalysts.

Cyclic voltammetry (CV) was performed in N_2 saturated 0.1 M $HClO_4$. For high voltage corrosion resistance characterisation of the support, 6000 cycles were performed between 1.0 V and 1.6 V with a scan rate of 100 mV s^{-1}.[41] After every 100 cycles, one cycle between 0.025 V and 1.2 V with a scan rate of 20 mV s^{-1} was performed to determine the electrochemical surface area (ECSA). Its calculation was based on hydrogen desorption peaks in the range 0.05 V to 0.4 V *vs.* RHE after double-layer correction, assuming a monolayer hydrogen adsorption charge of 210 µC cm^{-2} for the Pt surface. The ORR curves were recorded using linear sweep voltammetry at 1600 rpm in O_2 saturated 0.1 M $HClO_4$, varying the potential from 0.1 V to 1.2 V *vs.* RHE at a scan rate of 20 mV s^{-1}. The curves obtained were later background and IR corrected. Mass (MA) and specific activity (SA) values were calculated by dividing the kinetic currents obtained applying the Koutecky–Levich equation by the mass of Pt deposited onto the RDE or the Pt ECSA, respectively.

Results and discussion

Morphological and structural characterisation of electrospun doped-SnO_2

In this work, the doping percentages of Nb and Sb doped SnO_2 electrospun materials were fixed at 5 at% for Nb (NTO) and

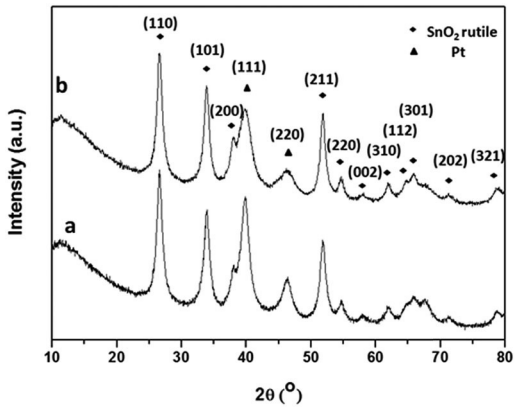

Fig. 1 XRD diffractograms of (a) Pt/NTO and (b) Pt/ATO.

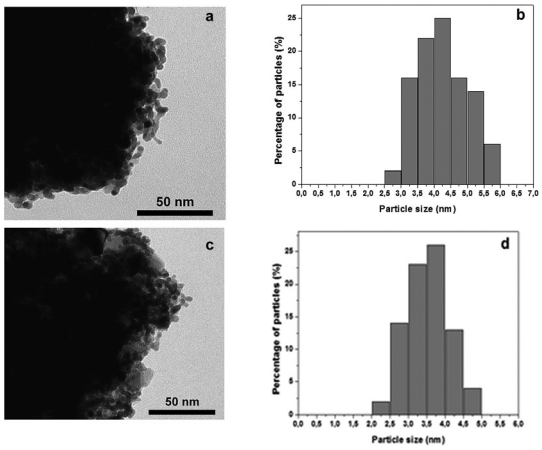

Fig. 2 TEM images of (a) Pt/NTO and (c) Pt/ATO and their corresponding Pt size distribution histograms (b and d).

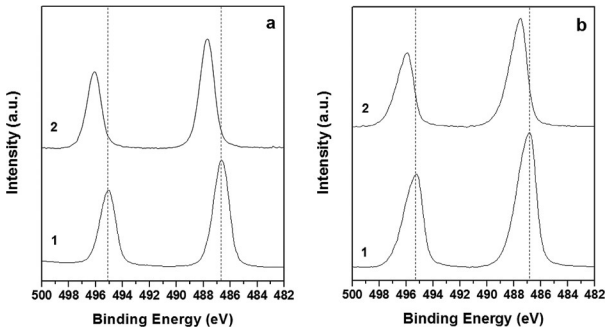

Fig. 3 XPS core level spectra of Sn3d for (a) NTO support (1) and Pt/NTO (2) and (b) ATO support (1) and Pt/ATO (2).

10 at% for Sb (ATO), as they correspond to the maximum observed electrical conductivity[37,40] of these metal oxides (0.021 and 1 S cm^{-1} at 20 ıC, respectively), of crucial importance for the envisaged application. The presence of Nb and Sb heteroatom promotes the formation of fibre-in-tube structures with an average tube diameter of 170 nm.

Analysis of the XRD patterns showed that all diffraction peaks correspond to polycrystalline rutile cassiterite tin oxide (Fig. 1). Niobium and antimony ions, due to their comparable ionic radii (0.69, 0.69, 0.74 for Sn^{4+}, Nb^{5+} and Sb^{5+}, respectively)[18] and their similar outer shell electronic configurations, are able to replace tin(IV) ions in the SnO_2 lattice without significant cell volume variations. The average crystallite size estimated from the Scherrer equation was 15.8 nm for NTO and 16.5 nm for ATO, which is in concordance with the TEM results.

Morphological and structural characterisation of Pt/doped-SnO_2

Pt nanoparticles prepared by the microwave-assisted polyol method were homogeneously dispersed onto the loose-tubes with an average diameter of 4.1 and 3.5 nm for Nb and Sb doped SnO_2 hollow fibres respectively, and in neither case was any aggregation observed (Fig. 2).

These results are in agreement with the expected crystallite size increase of Pt nanoparticles[37,40] brought about by the modification of the parameters of the microwave-assisted reaction.

In addition to the diffraction lines arising from tetragonal cassiterite SnO_2, the XRD pattern of the Pt/doped-SnO_2 materials (Fig. 1) also exhibits those assigned to the face-centred cubic structure of Pt (2y = 39.7, 46.2 and 67.4ı, JCPDS 004-0802). Applying the Scherrer equation to the Pt(111) peak gave an average diameter of the Pt crystallites on NTO and ATO of 4.5 and 3.8 nm respectively, in full agreement with TEM results. X-ray fluorescence analysis provided a Pt loading of 33 wt% on NTO and 37 wt% on ATO.

Surface analysis of doped-SnO_2 and Pt/doped-SnO_2

X-ray photoelectron spectroscopy (XPS) was carried out to investigate the surface chemical state of the Pt/doped-SnO_2 electrocatalysts. In particular, the analysis was performed on all the elements (Sn, Nb or Sb, O and Pt) present in the pristine supports and Pt catalysed materials.

In Fig. 3 are depicted the XPS spectra of the Sn3d core level. For the bare supports (Fig. 3-1), the binding energies of the $Sn3d_{5/2}$ and $Sn3d_{3/2}$ doublet are 486.6 and 495.0 eV for NTO (1-a), and 486.9 eV and 495.3 eV and ATO (1-b) and, considering the peak position and spin–orbit splitting of 8.4 eV, they are assigned to the highest oxidation state of Sn, *i.e.* IV.[42,43] Nevertheless, it is agreed that these features alone are not sufficient to distinguish Sn^{4+} from Sn^{2+} species. In a previous study on the same electrospun materials undoped and doped with Nb, other data including Sn/O stoichiometric ratio and Auger spectra were taken into account and led to the conclusion that the material surface also comprises oxygen-deficient SnO_2, and thus Sn^{2+} in addition to Sn^{4+}.[40]

The binding energy of the Sn3d doublet presents a 0.3 eV shift and peak asymmetry in ATO (Fig. 3-1-b) compared to NTO (Fig. 3-1-a), which may be ascribed to the different local chemical and physical environments,[44] due to higher atomic concentration of the doping agent (10 at% Sb *vs.* 5 at% Nb). The Sn3d high-resolution spectra of the catalysed supports, Pt/NTO (a) and Pt/ATO (b) are shown in Fig. 3-2.

When Pt nanoparticles are deposited onto the tin oxide loose-tubes, the Sn3d peaks are moved to higher energy by a

significant value of 1 eV. As already reported for other metal/oxide materials,[24,45] this BE shift may be attributed to the strong metal–support interaction between Pt and SnO_2. This interaction gives rise to charge transfer from tin to platinum, which induces a partial positive charge on tin and a subsequent local increase of the electron density on Pt. In some cases, a downshift instead of an increase in BE values was reported for the metal oxide as well as for the deposited metal, which then might involve not only charge transfer effects, but also changes in the lattice parameter due to alloy formation.[7,8]

The same effect was observed at the heteroatoms substituting tin in the lattice, *i.e.* Nb and Sb (Fig. 4 and 5).

The bare NTO support (Fig. 4-1) gives an XPS spectrum comprising an $Nb3d_{5/2}/Nb3d_{3/2}$ doublet, with binding energies of 207.2/210.0 eV, which is consistent with the presence of Nb(v),[21,40,46] and which corroborates the p-type doping of the metal oxide and the electrical conductivity increase. This doublet is shifted to higher energy by 1 eV in the spectrum of Pt/NTO (Fig. 4-2), compared to the bare material, which indicates that niobium ions as well as tin are both involved in electron donation to Pt.

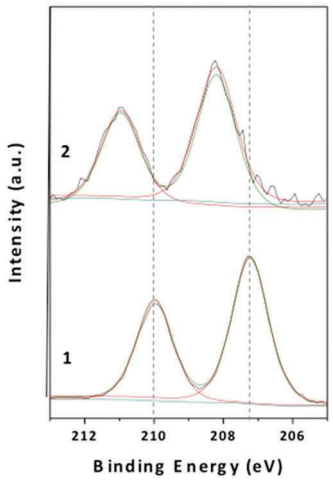

Fig. 4 XPS core level spectra of Nb3d for NTO electrocatalyst support (1) and Pt/NTO (2).

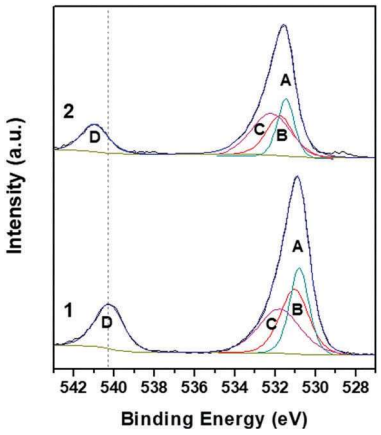

Fig. 5 XPS core level spectra of Sb3d and O1s for ATO (1) and Pt/ATO (2).

This phenomenon induces a partial positive charge on niobium, shifting its binding energy to higher values.[47,48]

The Nb/Sn atomic ratio given by XPS is 0.036. This is lower than expected for 5 at% doping due to a gradient of heteroatom distribution in the loose-tubes being higher in the inner fibres and lower on the outer tubes.[40] A shift to higher BE values was also observed when using Sb dopant. The XPS high-resolution spectra of the Sb3d region for bare (1) and catalysed ATO (2) are displayed in Fig. 5. This region partially overlaps with that of O1s at low binding energies. In Fig. 5-1 it is thus easily possible to attribute the peak at 540.2 eV in the ATO spectrum to the $Sb3d_{3/2}$ of Sb(v),[49] while for the $3d_{5/2}$ a peak deconvolution is needed to separate antimony and oxygen contributions. The broad peak between 528 and 535 eV can be decomposed into three contributions. That at 531.0 eV (band B) is the $Sb3d_{5/2}$ peak of Sb(v),[50–52] while the two others correspond to O1s signals, the peak at 530.8 eV (band A) being attributed to O^{2-} ions in an oxide lattice structure, and that at 531.7 eV (band C) to H_2O, OH or CO surface-adsorbed species.[53,54] Similar results for O1s peaks are obtained for NTO (Fig. 6) with a slight downshift probably due to the lower doping amount: the peak at 530.5 eV can be attributed to the metal oxide, and the peak at 531.4 eV to hydroxyl species at the material surface.

The spectrum recorded on Pt/ATO (Fig. 5-2) shows a 0.7 eV shift to higher energy for the Sb3d doublet, which is compatible with the SMSI between Pt and ATO,[52] already demonstrated by Sn and Nb peak analysis. The Sb/Sn ratio value of 0.17 is greater than expected for a 10 at% doping, showing a certain segregation of antimony at the SnO_2 surface.[26] The O1s peaks in Pt/ATO (Fig. 6-2) as well as in Pt/NTO (Fig. 5-2) are also shifted to higher binding energies (531.4 eV and 532.2 eV for Pt/ATO, and 531.2 and 532.2 eV for Pt/NTO).

This phenomenon has not been yet reported and may arise from the probable participation of oxygenated species in the charge transfer to Pt. A 10–20% increase of the contribution at high energy corresponding to oxygen bound to metal hydroxides or adsorbed hydrated species is seen when passing from the bare to the catalysed support, which may be related to the adsorption of such species on the Pt surface, in perfect agreement with the data of Fig. 7 that will be discussed below.

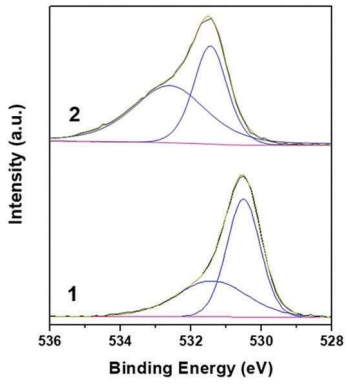

Fig. 6 XPS core level spectra of O1s for NTO (1) and Pt/NTO (2).

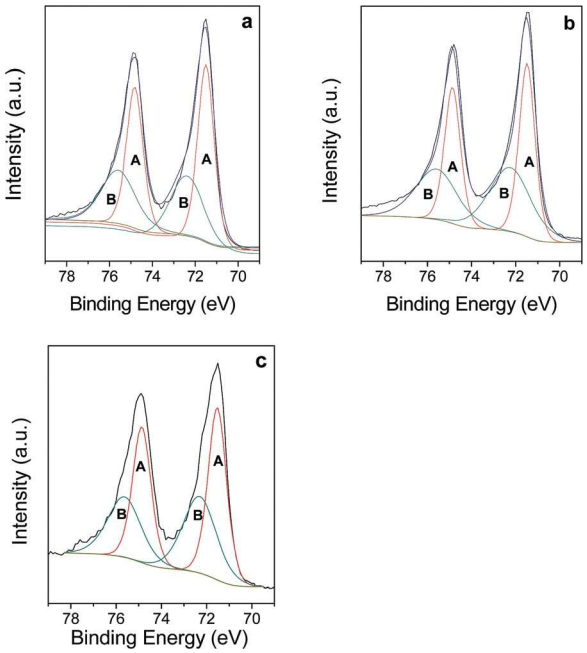

Fig. 7 XPS core level spectra of Pt4f for Pt/NTO (a), Pt/ATO (b) and Pt/C (c).

In Fig. 7 are displayed the Pt4f region in Pt/NTO (a) and Pt/ATO (b), and a Pt/C material (c) comprising a commercial carbon support (Vulcan XC-72R) and Pt nanoparticles synthesised and deposited on it in the same conditions as for the oxides. A $Pt4f_{7/2}/Pt4f_{5/2}$ doublet at 71.4/74.7 eV (A bands) is observed for the Pt/doped-SnO_2 (a, b), indicating that Pt is present in the metallic form. A further contribution is given by a second doublet at higher energy (B bands at 72.3 and 75.6 eV) corresponding to PtO_{ads} and/or $Pt(OH)_2$[55] due to partial surface oxidation of the Pt metal nanoparticles. Oxidised Pt was 42% and 44% of the total Pt for Pt/NTO and Pt/ATO, respectively, which qualitatively agrees with the increase in the peak of adsorbed hydroxyl species in the O1s spectra of Fig. 4 and 5. The signals for Pt4f for both samples (Fig. 7a and b) exhibit a slight downshift (0.1 eV) compared to the Pt/C material (71.5 eV, Fig. 7c). This shift is higher than that of other carbon-supported Pt catalysts (71.55[56] or 71.8 eV[12]), which is consistent with the existence of an SMSI between Pt and SnO_2, since charge transfer from the metal oxide to platinum enhances electron density on the latter, so shifting the Pt4f bands to lower energy.[12,17,30,57–60]

In other studies, X-ray absorption spectroscopy measurements showed that the decrease in the d-band vacancies of Pt may be attributed to the easier electron donation from the doped metal oxide support to the metallic Pt.[59]

Electrochemical characterisation of Pt/doped-SnO_2

Cyclic voltammograms of the Pt/doped SnO_2 and HiSPEC 9100 l Pt/C electrocatalyst materials are depicted in Fig. 8a, where the hydrogen adsorption/desorption peaks and Pt oxide formation and reduction are clearly seen. ECSA values were derived from the hydrogen desorption sweep, giving 47, 44 and 78 $m^2\ g^{-1}$, for Pt/NTO, Pt/ATO, and Pt/C respectively (Table 1).

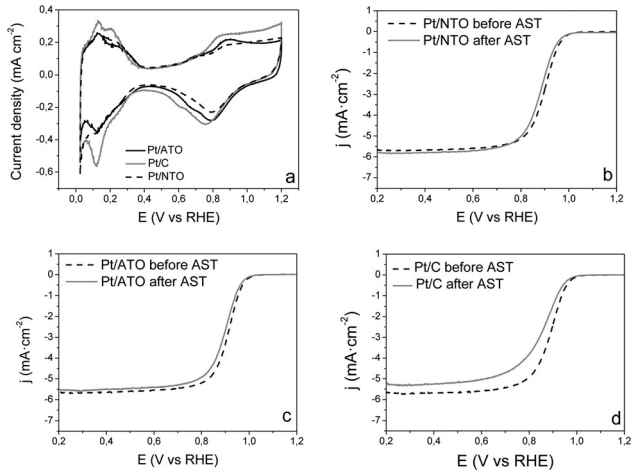

Fig. 8 Cyclic voltammograms in N_2 saturated $HClO_4$ (a) and ORR polarisation curves measured at 1600 rpm of the Pt/NTO (b), Pt/ATO (c) and Pt/C (d) electrocatalysts.

These values are higher than those previously reported for Pt/doped-SnO_2 loose-tubes (27 and 31 $m^2\ g^{-1}$),[37,40] and we attribute this to the thermal post-treatment leading to higher accessible metal surface. These values lie midway in the range of ECSAs (18 to 81 $m^2\ g^{-1}$) reported for Pt/doped-SnO_2 materials obtained *via* other synthetic routes.[18–20,22,23,26,61] They are, nevertheless, lower than those calculated on a geometric basis (70–80 $m^2\ g^{-1}$), and than that of the commercial Pt/C. Pt nanoparticle encapsulation taking place on reducible metal oxide supports and generally associated with the strong metal–support interaction discussed above[6,62,63] is the probable explanation for lower ECSA in Pt/SnO_2. The electrical conductivity of the support, lower than that of carbon, can also lead to a reduced ECSA as some particles may not be active as electrically disconnected. The relatively low specific surface area of the SnO_2 based supports (35–50 $m^2\ g^{-1}$)[37,40] may also be responsible for the low Pt utilisation.[64]

In the voltammograms of the tin oxide based electrocatalysts a small peak is discernible at 0.71 V per RHE. Earlier investigations of adsorption of p-block elements on Pt and recent results on similar Pt/ATO electrocatalyst suggest the assignment of this peak to a change in the degree of oxidation of Sn atoms adsorbed on the Pt surface.[26,65]

The ORR mass (MA) and specific activity (SA) values of Pt deposited on the doped SnO_2 loose-tubes and the commercial carbon-based electrocatalyst were evaluated, and the corresponding ORR polarisation curves are presented in Fig. 8b–d. Optimisation of the synthetic route to the Pt/SnO_2 electrocatalysts led to a significant improvement in mass activity compared to that previously reported for Pt/doped SnO_2 electrospun loose-tubes (0.034 A mg_{Pt}^{-1} for Pt/NTO[36] and 0.14 A mg^{-1} Pt for Pt/ATO[37] at 0.9 V per RHE), since the MA values at 0.9 V per RHE are 0.18, 0.20 and 0.27 A mg_{Pt}^{-1} for Pt/C, Pt/NTO and Pt/ATO, respectively (Table 1), and 0.59, 0.81 and 1.26 A mg^{-1} Pt at 0.85 V per RHE. Specific and mass activities of Pt supported on both tin oxide supports was higher than on carbon and, notably, the electrocatalytic activity of Pt/ATO loose-tubes is one of the

Table 1 Electrochemical surface area (ECSA) and ORR mass activity (MA) and specific activity (SA) values at 0.9 V per RHE of the different electrocatalysts obtained before and after the corrosion resistance characterisation of the support

Catalyst	ECSA ($m^2\ g^{-1}$ Pt) before [and after AST]	ORR $MA_{0.9V}$ ($A\ mg^{-1}$ Pt) before [and after AST]	ORR $SA_{0.9V}$ ($mA\ cm^{-2}$ Pt) before [and after AST]
Pt/NTO	47 [40]	0.20 [0.13]	426 [325]
Pt/ATO	44 [34]	0.27 [0.17]	614 [500]
Pt/C	78 [34]	0.18 [0.09]	231 [265]

highest values reported so far for Pt/metal oxide electrocatalysts.[12,18–20,22–24,26,39,61] Such electrocatalytic activity enhancement can be ascribed to the strong metal–support interaction between Pt and the doped metal oxide which greatly modifies the electronic structure of platinum, the latter promoting electrocatalysis of the metal nanoparticles.[6,7,62,66] Indeed, the thermal treatment performed after Pt deposition may not only free the metal surface from residual surfactant thus improving the interface with the support, but also enhance the particle adhesion onto it and subsequently the SMSI. No similar effect took place on the carbon support, and mass activity values in agreement with previous results[37] and with the literature were founded for Hispec Pt/C.[67,68]

In order to investigate the electrochemical stability of the various support materials (doped SnO_2 *vs.* carbon), an accelerated stress test (AST) at high voltage (1.0–1.6 V per RHE) was applied and the variation in ECSA and ORR activity was monitored. The results are shown in Table 1, Fig. 8b–d and Fig. S1 (see ESI†).

After 6000 cycles between 1.0 and 1.6 V, the drop in electrochemical surface area, mass and specific activity was lower for the oxide-based electrodes than for the carbon-based commercial electrode. Clearly the Pt/C cathode is less resistant to corrosion at high cell voltage than the Pt/metal oxide[12,19,22,24,61] The oxide support on the one hand possesses high corrosion resistance[36,69] (see ESI,† Fig. S2), and on the other hand favours anchoring of the Pt nanocatalyst *via* the strong electronic interaction demonstrated by the XPS study. The ECSA and ORR MA loss are similar for both Pt/tin oxide electrocatalysts, but are slightly lower for the NTO-based one (ECSA —16% *vs.* —23% and ORR MA —33% *vs.* —37%). For the Pt/ATO electrocatalyst, the mass activity after the high potential AST is practically the same as that of the commercial Pt/C before use. This provides a clear evidence that the doped SnO_2-loose-tubes are stable under high potential conditions and retain their high ORR electroactivity.

Conclusions

The ORR mass activity of Pt/Nb– and Sb–SnO_2 loose-tubes materials with *ca.* 4 nm Pt particles prepared by a microwave assisted polyol synthesis particles and heat treated to remove residual surfactant is the highest reported for tin oxide-based electrocatalysts, being 0.27 A mg^{-1} Pt for Pt/ATO at 0.9 V per RHE. The electrochemical stability of these catalysts is excellent up to 1.6 V with *ca.* 80% ECSA and *ca.* 65% mass activity retention. This property enhancement is considered to result from the strong interaction between Pt and doped SnO_2. A detailed XPS study provided evidence for the occurrence of charge transfer from tin (and its substituting ions) towards platinum, which is responsible for the enhanced electrocatalytic activity and nanocatalyst anchoring. While doped SnO_2 loose-tubes show excellent electrocatalytic activity and high stability, their textural and surface properties provide new challenges for the development of PEMFC cathode catalyst layers, and for fuel cell water management.

Conflicts of interest

There are no conflicts to declare.

Acknowledgements

Funding from the European Research Council under the European Union's Seventh Framework Programme (FP/2007–2013)/ERC Grant Agreement no. 306682 SPINAM is gratefully acknowledged. SC thanks the French IUF for its support. I. J.-M. acknowledges the financial support from the French National Research Agency (ANR-12-PRGE-0007).

References

1 L. Du, Y. Shao, J. Sun, G. Yin, J. Liu and Y. Wang, *Nano Energy*, 2016, 29, 314–322.
2 Y.-J. Wang, D. P. Wilkinson and J. Zhang, *Chem. Rev.*, 2011, 111, 7625–7651.
3 H. Lv and S. Mu, *Nanoscale*, 2014, 6, 5063–5074.
4 P. J. Kulesza, K. Miecznikowski, B. Baranowska, M. Skunik, A. Kolary-Zurowska, A. Lewera, K. Karnicka, M. Chojak, I. Rutkowska, S. Fiechter, P. Bogdanoff, I. Dorbandt, G. Zehl, R. Hiesgen, E. Dirk, K. S. Nagabhushana and H. Boennemann, *J. Appl. Electrochem.*, 2007, 37, 1439–1446.
5 L. Timperman, A. S. Gago and N. Alonso-Vante, *J. Power Sources*, 2011, 196, 4290–4297.
6 S. J. Tauster, *Acc. Chem. Res.*, 1987, 20, 389–394.
7 J. Ma, A. Habrioux and N. Alonso-Vante, *ChemElectroChem*, 2014, 1, 37–46.
8 A. Lewera, L. Timperman, A. Roguska and N. Alonso-Vante, *J. Phys. Chem. C*, 2011, 115, 20153–20159.
9 L. Timperman and N. Alonso-Vante, *Electrocatalysis*, 2011, 2, 181–191.
10 J. Zhang, M. Zhang, Z. Jin, J. Wang and Z. Zhang, *Appl. Surf. Sci.*, 2012, 258, 3991–3999.
11 N. R. Elezovic, B. M. Babic, V. R. Radmilovic, L. M. Vracar and N. V. Krstajic, *Electrochim. Acta*, 2009, 54, 2404–2409.
12 M. Yin, J. Xu, Q. Li, J. O. Jensen, Y. Huang, L. N. Cleemann, N. J. Bjerrum and W. Xing, *Appl. Catal., B*, 2014, 144, 112–120.
13 C. Marichy, G. Ercolano, G. Caputo, M. G. Willinger, D. Jones, J. Rozi`ere, N. Pinna and S. Cavaliere, *J. Mater. Chem. A*, 2016, 4, 969–975.

14 Y.-J. Wang, D. P. Wilkinson, A. Guest, V. Neburchilov, R. Baker, F. Nan, G. A. Botton and J. Zhang, *J. Power Sources*, 2013, 221, 232–241.

15 N. Elezovi´c, B. Babi´c, L. Gaji´c-Krstaji´c, V. Radmilovi´c, N. V. Krstaji´c and L. J. Vra˘car, *J. Power Sources*, 2010, 195, 3961–3968.

16 I. Savych, J. Bernard D'Arbigny, S. Subianto, S. Cavaliere, D. J. Jones and J. Rozi`ere, *J. Power Sources*, 2014, 257, 147–155.

17 V. B. Hughes and B. D. McNicol, *J. Chem. Soc., Faraday Trans. 1*, 1979, 75, 2165.

18 Y. Senoo, K. Kakinuma, M. Uchida, H. Uchida, S. Deki and M. Watanabe, *RSC Adv.*, 2014, 4, 32180.

19 K. Kakinuma, Y. Chino, Y. Senoo, M. Uchida, T. Kamino, H. Uchida, S. Deki and M. Watanabe, *Electrochim. Acta*, 2013, 110, 316–324.

20 G. Cognard, G. Ozouf, C. Beauger, I. Jim´enez-Morales, S. Cavaliere, D. Jones, J. Rozi`ere, M. Chatenet and F. Maillard, *Electrocatalysis*, 2017, 8, 51–58.

21 G. Ozouf and C. Beauger, *J. Mater. Sci.*, 2016, 51, 5305–5320.

22 F. Takasaki, S. Matsuie, Y. Takabatake, Z. Noda, A. Hayashi, Y. Shiratori, K. Ito and K. Sasaki, *J. Electrochem. Soc.*, 2011, 158, B1270.

23 T. Tsukatsune, Y. Takabatake, Z. Noda, T. Daio, A. Zaitsu, S. M. Lyth, A. Hayashi and K. Sasaki, *J. Electrochem. Soc.*, 2014, 161, F1208–F1213.

24 M. Dou, M. Hou, F. Wang, D. Liang, Q. Zhao, Z. Shao and B. Yi, *J. Electrochem. Soc.*, 2014, 161, F1231–F1236.

25 J. Suffner, S. Kaserer, H. Hahn, C. Roth and F. Ettingshausen, *Adv. Energy Mater.*, 2011, 1, 648–654.

26 G. Cognard, G. Ozouf, C. Beauger, L. Dubau, M. Lo´pez-Haro, M. Chatenet and F. Maillard, *Electrochim. Acta*, 2017, 245, 993–1004.

27 K. Kanda, Z. Noda, Y. Nagamatsu, T. Higashi, S. Taniguchi, S. M. Lyth, A. Hayashi and K. Sasaki, *ECS Electrochem. Lett.*, 2014, 3, F15–F18.

28 M. Sudan Saha, R. Li, M. Cai and X. Sun, *Electrochem. Solid-State Lett.*, 2007, 10, B130.

29 C. Du, M. Chen, X. Cao, G. Yin and P. Shi, *Electrochem. Commun.*, 2009, 11, 496–498.

30 G. Samjesk´e, S. Nagamatsu, S. Takao, K. Nagasawa, Y. Imaizumi, O. Sekizawa, T. Yamamoto, Y. Uemura, T. Uruga and Y. Iwasawa, *Phys. Chem. Chem. Phys.*, 2013, 15, 17208–17218.

31 H. Lv, N. Cheng, T. Peng, M. Pan and S. Mu, *J. Mater. Chem.*, 2012, 22, 1135–1141.

32 K. Sasaki, F. Takasaki, Y. Shiratori, Z. Noda, K. Sasaki, F. Takasaki, Y. Shiratori and Z. Noda, *Proc. WHEC2010*, 2010, 103–108.

33 A. Masao, S. Noda, F. Takasaki, K. Ito and K. Sasaki, *Electrochem. Solid-State Lett.*, 2009, 12, B119–B122.

34 Q. Du, J. Wu and H. Yang, *ACS Catal.*, 2014, 4, 144–151.

35 M. Dou, M. Hou, D. Liang, W. Lu, Z. Shao and B. Yi, *Electrochim. Acta*, 2013, 92, 468–473.

36 I. Savych, S. Subianto, Y. Nabil, S. Cavaliere, D. Jones and J. Rozi`ere, *Phys. Chem. Chem. Phys.*, 2015, 17, 16970–16976.

37 S. Cavaliere, I. Jim´enez-Morales, G. Ercolano, I. Savych, D. Jones and J. Rozi`ere, *ChemElectroChem*, 2015, 2, 1966–1973.

38 U.S. Department of Energy, *Fuel Cell Technical Team Roadmap*, 2013.

39 Y. Senoo, K. Taniguchi, K. Kakinuma, M. Uchida, H. Uchida, S. Deki and M. Watanabe, *Electrochem. Commun.*, 2015, 51, 37–40.

40 S. Cavaliere, S. Subianto, I. Savych, M. Tillard, D. J. Jones, J. Rozi`ere and D. J. Jones, *J. Phys. Chem. C*, 2013, 117, 18298–18307.

41 S. S. Kocha, Y. Garsany and D. Myers, *DOE Webinar*, 2013.

42 V. Senthilkumar, P. Vickraman, M. Jayachandran and C. Sanjeeviraja, *J. Mater. Sci.: Mater. Electron.*, 2009, 21, 343–348.

43 Q. Liu, L. Zhang, J.-F. Chen and Y. Le, *Mater. Lett.*, 2014, 137, 339–342.

44 A. R. Babar, S. S. Shinde, A. V. Moholkar, C. H. Bhosale, J. H. Kim and K. Y. Rajpure, *J. Alloys Compd.*, 2010, 505, 416–422.

45 S. Ntais, R. J. Isaifan and E. A. Baranova, *Mater. Chem. Phys.*, 2014, 148, 673–679.

46 M.-Y. Tse, X. Wei and J. Hao, *Phys. Chem. Chem. Phys.*, 2016, 18, 24270–24277.

47 H. J. Chun, D. B. Kim, D. H. Lim, W. D. Lee and H. I. Lee, *Renewable Energy*, 2010, 35, 6399–6408.

48 X. Liu, X. Wu and K. Scott, *Catal. Sci. Technol.*, 2014, 3891–3898.

49 F. Garbassi, *Surf. Interface Anal.*, 1980, 2, 165–169.

50 R. Berenguer, J. M. Sieben, C. Quijada and E. Morallo´n, *ACS Appl. Mater. Interfaces*, 2014, 6, 22778–22789.

51 C. Bernard, I. Lyon and R. Berjoan, *J. Sol-Gel Sci. Technol.*, 1997, 81, 75–81.

52 F. Montilla, E. Morallo´n, A. De Battisti, S. Barison, S. Daolio and J. L. V´azquez, *J. Phys. Chem. B*, 2004, 108, 15976–15981.

53 K. D. Bomben, J. F. Moulder, P. E. Sobol and W. F. Stickle, *Handbook of X-ray photoelectron spectroscopy. A reference book of standard spectra for identification and interpretation of XPS data*, Physical Electronics, Eden Prairie, MN, 1995.

54 N. R. Elezovic, V. R. Radmilovic, J. Kovac, B. M. Babic, L. M. Gaijic-Krstajic and N. V. Krstajic, *RSC Adv.*, 2015, 5, 15923–15929.

55 F. Raynal, A. Etcheberry, S. Cavaliere, V. No¨el and H. Perez, *Appl. Surf. Sci.*, 2006, 252, 2422–2431.

56 A. Shukla, A. Arico`, K. El-Khatib, H. Kim, P. Antonucci and V. Antonucci, *Appl. Surf. Sci.*, 1999, 137, 20–29.

57 N. Zhang, S. Zhang, C. Du, Z. Wang, Y. Shao, F. Kong, Y. Lin and G. Yin, *Electrochim. Acta*, 2014, 117, 413–419.

58 K. Lee, I. Park, Y. Cho, D. Jung, N. Jung, H. Park and Y. Sung, *J. Catal.*, 2008, 258, 143–152.

59 V. T. Thanh, Ho, K. C. Pillai, H.-L. Chou, C.-J. Pan, J. Rick, W.-N. Su, B.-J. Hwang, J.-F. Lee, H.-S. Sheu and W.-T. Chuang, *Energy Environ. Sci.*, 2011, 4, 4194.

60 J. C. Colmenares, A. Magdziarz, M. A. Aramendia, A. Marinas, J. M. Marinas, F. J. Urbano and J. A. Navio, *Catal. Commun.*, 2011, 16, 1–6.

61 N. R. Elezovic, B. M. Babic, V. R. Radmilovic and N. V. Krstajic, *J. Electrochem. Soc.*, 2013, 160, F1151–F1158.

62 V. A. de la Pena O'Shea, M. C. Alvarez Galvan, A. E. Platero Prats, J. Campos-Martin and J. Fierro, *Chem. Commun.*, 2011, 47, 7131–7133.

63 J. C. Matsubu, S. Zhang, L. DeRita, N. S. Marinkovic, J. G. Chen, G. W. Graham, X. Pan and P. Christopher, *Nat. Chem.*, 2017, 9, 120–127.
64 M. Yin, J. Xu, Q. Li, J. O. Jensen, Y. Huang, L. N. Cleemann, N. J. Bjerrum and W. Xing, *Appl. Catal., B*, 2014, 144, 112–120.
65 H. Massong, S. Tillmann, T. Langkau, E. A. Abd El Meguid and H. Baltruschat, *Electrochim. Acta*, 1998, 44, 1379–1388.
66 L. Xiong and A. Manthiram, *Electrochim. Acta*, 2004, 49, 4163–4170.
67 N. P. Lebedeva, A. S. Booij and G. J. Janssen, *ECS Trans.*, 2008, 16, 2083–2092.
68 S. H. Joo, C. Pak, D. J. You, S. A. Lee, H. I. Lee, J. M. Kim, H. Chang and D. Seung, *Electrochim. Acta*, 2006, 52, 1618–1626.
69 B. Rodr´ıguez-Garc´ıa, A. Reyes Carmona, I. Jim´enez-Morales, M. Blasco-Ahicart, S. Cavaliere, M. Dupont, D. Jones, J. Rozi`ere, J. Gal´an-Mascar´os and F. Jaouen, *Sustainable Energy Fuels*, 2018, 2, 589–597.